Figure 1. CD3 versus CD7 plots in flow cytometric analysis of patients who are asymptomatic HTLV-I carriers (ACs) and have various clinical subtypes of adult T-cell leukemia-lymphoma (ATL) suggest disease progression in HTLV-I infection. (A) Flow cytometric profile of an AC, various clinical subtypes of ATL (smoldering, chronic, and acute), and a normal control. Representative cases of CD3 versus CD7 plots in CD4$^+$ cells are shown. (B) A two-dimensional plot of AC cases showing the percentage of the D and L subpopulations by flow cytometry. AC cases were divided into two groups according to HTLV-I VL (greater or less than 4%). The border line (45% of D+L subpopulations) between Group 1 and 2 was set based on proviral load (VL). All AC cases with less than 4% VL were included in Group 1. All AC cases included in Group 2 had greater than 4% VL. VL<4%: n = 21; VL>4%: n = 19. All VL data in this figure were provided from the database of the Joint Study on Predisposing Factors of ATL Development (JSPFAD). (C) A two-dimensional plot of all patients showing the percentage of the D and L subpopulations. The smoldering type was divided into two categories: smoldering type with greater than 5% abnormal lymphocytes and smoldering type with less than 5% abnormal lymphocytes with skin manifestation. The two diagonal dotted lines indicate 45% and 100% of D+L subpopulations (*i.e.,* 55% and 0% of the H subpopulation). Data were categorized into three groups.
doi:10.1371/journal.pone.0053728.g001

CAGTAGGGCGTGACGATGTA-3'), FAM-labeled probe at 0.1 μM (5'- CTGTGTACAAGGCGACTGGTGCC-3'), and 1× TaqMan Universal PCR master mix (Applied Biosystems), was subjected to 50 cycles of denaturation (95°C, 15 seconds) and annealing to extension (60°C, 1 minute), following an initial Taq polymerase activation step (95°C, 10 minutes). The RNase P control reagent (Applied Biosystems) was used as an internal control for calculating the input cell number (using VIC reporter dye). DNAs extracted from TL-Om1 and normal human PBMCs were used as positive and negative controls, respectively. The HTLV-I proviral load (%) was calculated as the copy number of the pX region per input cell number. To correct the deviation of

data acquired in each experiment, data from TL-Om1 (positive control) were adjusted to 100%, and the sample data were corrected accordingly by a proportional calculation.

Inverse long PCR

For clonality analysis, inverse long PCR was performed [17]. First, 1 μg of genomic DNA extracted from the FACS-sorted cells was digested with *Eco*RI and *Pst*I at 37°C overnight. Purification of DNA fragments was performed using a QIAEX2 gel extraction kit (Qiagen). The purified DNA was self-ligated with T4 DNA ligase (Takara Bio, Otsu, Japan) at 16°C overnight. The circular DNA obtained from the *Eco*RI digestion fragment was then digested
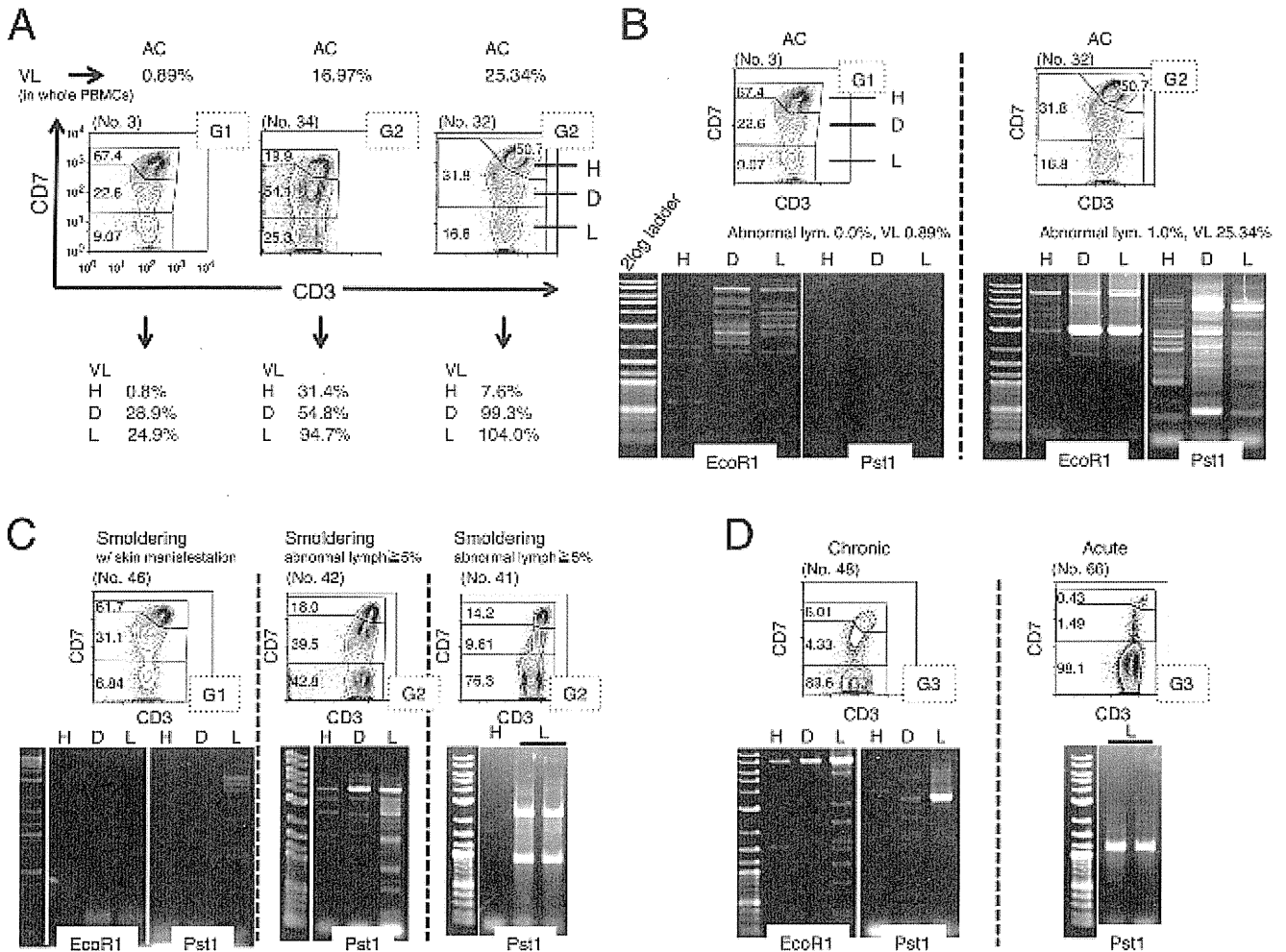
— 145 —

Figure 2. HTLV-I proviral load (VL) and clonality in each subpopulation, based on the CD3 versus CD7 plot. (A) The three subpopulations (H, D, L) based on the CD3 versus CD7 plot were subjected to fluorescence-activated cell sorting (FACS) and VL analysis. Three representative cases are shown. G1 or G2 in the dotted box indicates Group 1 or Group 2, categorized by the percentage of the D and L subpopulations, respectively. (B)–(D) Analysis of clonality in the three subpopulations based on the CD3 versus CD7 plot. Genomic DNA was extracted from FACS-sorted cells of each subpopulation and subjected to inverse long polymerase chain reaction (PCR). Representative data of two cases of AC (B), three cases of smoldering type, including one with skin manifestations (C), and cases of a chronic type and an acute type (D) are shown. PCR was performed in duplicate (black bars) in cases when a sufficient amount of DNA was obtained.
doi:10.1371/journal.pone.0053728.g002

with *Mlu*I, which cuts the pX region of the HTLV-I genome and prevents amplification of the viral genome. Inverse long PCR was performed using Takara LA *Taq* polymerase (Takara Bio). For the *Eco*RI-treated template, the forward primer was 5'-TGCCTGACCCTGCTTGCTCAACTCTACGTCTTTG-3' and the reverse primer was 5'-AGTCTGGGCCCT-GACCTTTTCAGACTTCTGTTTC-3'. For the *Pst*I-treated group, the forward primer was 5'-CAGCCCATTCTATAG-CACTCTCCAGGAGAG-3' and the reverse primer was 5'-CAGTCTCCAAACACGTAGACTGGGTATCCG-3. Each 50-µL reaction mixture contained 0.4 mM of each dNTP, 25 mM MgCl₂, 10× LA PCR buffer II containing 20 mM Tris-HCl and 100 mM KCl, 0.5 mM of each primer, 2.5 U LA *Taq* polymerase, and 50 ng of the processed genomic DNA. The reaction mixture was subjected to 35 cycles of denaturation (94°C, 30 seconds) and annealing to extension (68°C, 8 minutes). Following PCR, the products were subjected to electrophoresis on 0.8% agarose gels. In samples from which a sufficient amount of DNA was extracted, PCRs were performed in duplicate.

Results

CD3 versus CD7 profile in flow cytometry in various clinical subtypes of patients infected with HTLV-I

The clinical profiles of the 77 cases analyzed in this study are shown in Table 1. According to the gating procedure, as shown in Figure S1 [17], we constructed a CD3 versus CD7 plot of CD4⁺ cells in PBMCs of various clinical subtypes from patients infected with HTLV-I and normal controls. The three subpopulations ($CD3^{high}CD7^{high}$, $CD3^{dim}CD7^{dim}$, and $CD3^{dim}CD7^{low}$) observed are referred to as the H, D, and L subpopulations, respectively. Representative results for each clinical subtype of HTLV-I infection are shown in Figure 1A. Regarding the data for an acute-type patient (no. 66), the dominant population was the L subpopulation, in which we previously demonstrated that mono-clonal ATL cells are enriched [17]. Regarding the AC (no. 19), the CD3 versus CD7 profile was close to that of the normal control, although in some AC cases, such as no. 32, the profile differed from that of the normal control, because in contrast to case no. 19,
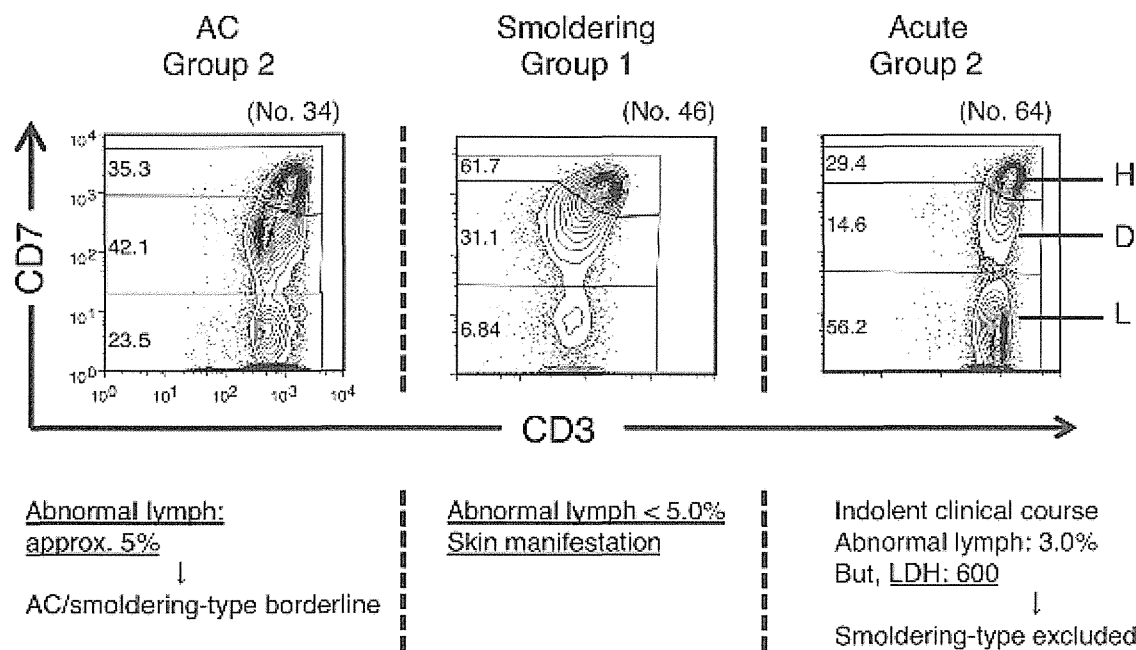
— 146 —

Figure 3. Study of exceptional cases categorized by proportion of the CD3^{dim}CD7^{dim} (D) and CD3^{dim}CD7^{low} (L) subpopulations. Left: An HTLV-I AC patient who was categorized in Group 2 in the D(%) versus L(%) plot. Middle: A patient with smoldering-type ATL who was categorized in Group 1. Right: A patient with acute-type ATL who was categorized in Group 2.
doi:10.1371/journal.pone.0053728.g003

these cases had increased D and L subpopulations. Regarding the data for indolent-type disease (smoldering and chronic), increases in the D and L subpopulations were intermediate between ACs and patients with acute-type disease. These representative flow cytometric data suggest that continuity in the CD3 versus CD7 profile seemed to exist among the various clinical subtypes of patients infected with HTLV-I.

The proportions of D and L subpopulations in all AC cases analyzed are shown in Figure 1B. Because the high HTLV-I proviral load (VL) in whole PBMCs, a VL of >4%, was reported to be a major risk indicator for progression to ATL [13], a border line was set based on VL. Group 1, the area under the diagonal line (D+L = 45%), included all AC cases with VLs of <4%. ACs with VLs of >4% were distributed between Groups 1 and 2. The proportions of D and L subpopulations in normal controls are shown in Figure S2. In this plot, all data for normal controls were distributed in Group 1. Data for all clinical subtypes are shown in Figure 1C. Most data for acute-type patients were located in the area beyond 80% of the L subpopulation and we designated this area as Group 3. Group 2, which is located between Group 1 and Group 3, included the majority of indolent-type (smoldering and chronic) cases. From these results, the three groups in the D(%) versus L(%) plot seemed to represent disease stage in each case.

Proviral load and clonality in each subpopulation in the CD3 versus CD7 plot

To further characterize each subpopulation (H, D, and L) in the CD3 versus CD7 plot, cells in each subpopulation were FACS-sorted and subjected to analysis of VL to determine the percentage of HTLV-I-infected cells in each subpopulation. Results for representative cases are shown in Figure 2A. The VL in whole PBMCs of an AC (no. 3) was low (0.89%). As expected, the VL in H, the major subpopulation, was low (0.8%). However, VLs in the D and L subpopulations were considerably higher (28.9% and

24.9%, respectively), indicating that HTLV-I-infected cells are relatively concentrated in these subpopulations. In the cases with high VLs in whole PBMCs (no. 32 with 25.34%; no. 34 with 16.97%), the VLs were also higher in the D and L subpopulations, and almost all cells in the L subpopulation were HTLV-I-infected.

In HTLV-I infection, progression to ATL requires several pathological steps, including clonal expansion [15]. To further characterize the three subpopulations based on the CD3 versus CD7 plot, we analyzed clonality in each subpopulation in patients with various clinical subtypes using the inverse long PCR method. Figure 2B shows two cases of AC. In the left case (no. 3), included in Group 1 in the D(%) and L(%) plot, multiple bands suggestive of multiple small clones were detected in the three subpopulations. However, no major band suggestive of a dominant clone was observed. In the right case (no. 32), included in Group 2, inverse long PCR of the FACS-sorted subpopulations suggested that the D and L subpopulations contained a major clone (Figure 2B). The D subpopulation had bands of the same size as those of the L subpopulation, indicating that the two distinct subpopulations contained a common major clone. Eleven cases of AC were included in Group 2. All three cases analyzed by Southern blotting (whole blood samples) were positive for clonal bands (Figure S3). In Figure 2C, data for three smoldering cases are shown. In case no. 46 (left), whose only manifestation was a skin eruption with few abnormal lymphocytes (less than 5% of white blood cells) in the peripheral blood, only faint minor bands suggestive of small clones were observed. In contrast, in the other two cases (nos. 42 and 41), intense bands suggestive of major clones were observed in both the D and L subpopulations. In no. 41 (right), weak bands were not visible, which suggested the selection of dominant clones. In Figure 2D, data for a chronic-type case and an acute-type case are shown. In both cases, intense bands in the L subpopulation suggest the existence of a major clone. The series of clonality analyses indicated that a major clone became more evident and the clinical
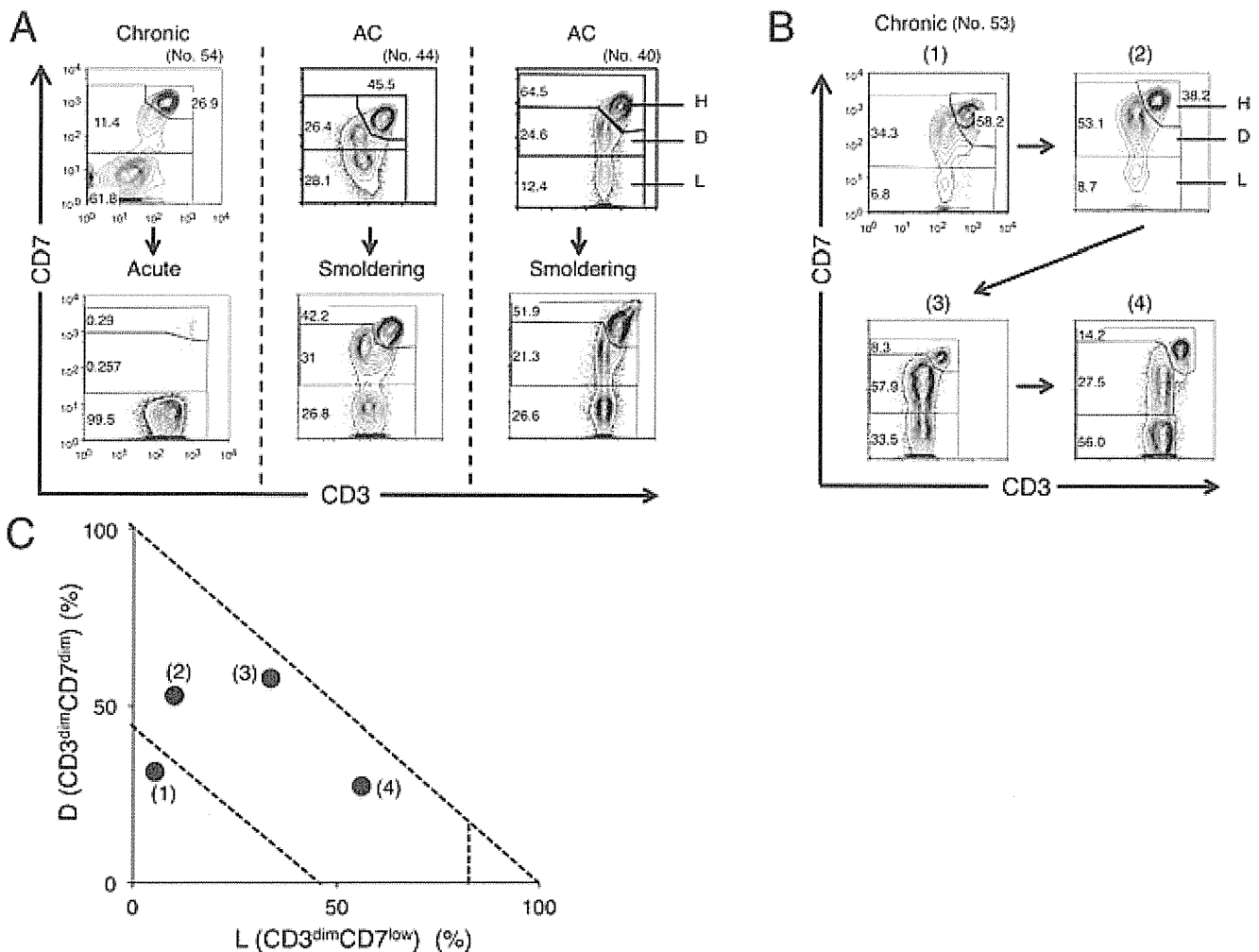
Figure 4. Alteration in the CD3 versus CD7 profile by flow cytometry in accordance with disease progression. (A) Change in the CD3 versus CD7 profile in representative cases. In all three cases shown, change in clinical data (e.g., abnormal lymphocyte, LDH) resulted in progression of the clinical subtype. (B) Change in the CD3 versus CD7 profile in a time course in the case of chronic-type ATL. Clinical data are shown in Table S1. (C) Flow cytometric data in (B) are summarized in the D(%) versus L(%) plot.
doi:10.1371/journal.pone.0053728.g004

stage became more advanced as the D and L subpopulations increased.

Clinical evaluation of exceptional cases categorized by proportions of the CD3^{dim}CD7^{dim} (D) and CD3^{dim}CD7^{low} (L) subpopulations

As noted above, the D(%) versus L(%) plot generally represented disease stage in HTLV-I infection. However, we observed one case of chronic-type disease and three cases of smoldering-type disease in Group 1 and three cases of acute-type disease in Group 2. Furthermore, some ACs with VLs of >4% were observed in Group 2. Representative data from these apparently exceptional cases are shown in Figure 3. On the left, a case of AC (no. 34) observed in Group 2 is shown. 4.7% of lymphocytes in this blood sample were abnormal and clonality analysis by Southern blotting showed oligoclonal bands suggestive of clones of substantial size (Figure S3). These clinical data suggest that the disease stage would be around the AC/smoldering borderline. In the middle, a case of a smoldering type (no. 46) observed in Group 1 is shown. In this case, the percentage of abnormal lymphocytes in the peripheral blood was only 1%, but she had a histologically proven ATL lesion

in the skin and was diagnosed with smoldering-type ATL. The other two smoldering cases categorized in Group 1 were the same as this case. These results indicate that ATL cells in these three smoldering cases infiltrated the skin, but not the peripheral blood. On the right, a case of acute-type disease categorized as Group 2 (no. 64) is shown. The clinical course of this patient was relatively indolent compared with typical acute-type disease. He had skin infiltration of ATL cells, but no lymph node swelling. However, LDH exceeded 1.5 times the upper limit of the normal range, which excludes a diagnosis of smoldering-type disease. Other acute-type cases categorized in Group 2 were diagnosed as such according to Shimoyama's criteria, but also had the same indolent clinical course as case no. 64. These cases should have been regarded as indolent ATL.

Changes in the CD3 versus CD7 profile in flow cytometry with disease progression

In several cases, we could obtain time-sequential samples (Figure 4). The patient (no. 54) shown on the left in Figure 4A progressed from chronic-type to acute-type disease. In flow cytometric analysis, decreases in the H and D subpopulations
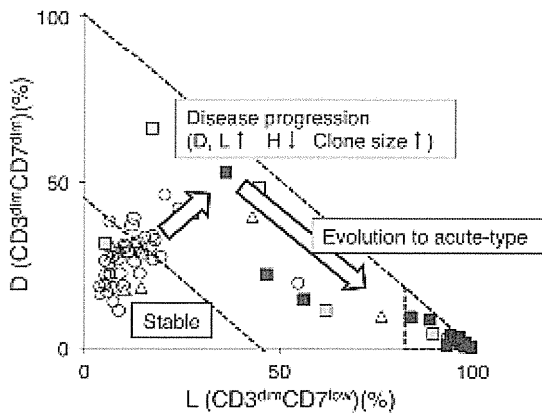
— 148 —

Figure 5. Summary of the study: the CD3 versus CD7 profile reflects progression of disease stage in patients infected with HTLV-I. In the percentage of D (CD3^{dim}CD7^{dim}) versus L (CD3^{dim} CD7^{low}) plot, Group 1 includes the majority of AC cases. As disease stage progresses, the CD3 versus CD7 profile then changes. With downregulation of CD3 and CD7, the D and L subpopulations increase gradually (Group 2). During this step, clones in the D and L subpopulations increase in size. Further accumulation of genetic alterations will result in rapid expansion of ATL clones—*i.e.*, evolution to acute-type ATL. In this step, the CD3 versus CD7 profile will progress from Group 2 to 3.
doi:10.1371/journal.pone.0053728.g005

and an increase in the L subpopulation were observed, indicating that disease progression correlated well with the change in the CD3 versus CD7 profile. The patients in the middle (no. 44) and on the right (no. 40) were included in Group 2 at the AC stage and later progressed to smoldering-type ATL. Although variation in the change of the flow cytometric profile was seen between these patients, the results suggest that ACs in Group 2 are at high risk of developing ATL.

The patient in Figure 4B (no. 53) was initially diagnosed with AC and later progressed to chronic-type ATL. Although the initial clinical course was stable, an increase in abnormal lymphocyte numbers was later observed, and low-dose VP-16 therapy (50 mg/day) was initiated because of hypoxemia due to lung infiltration of ATL cells. Table S1 and Figure 4C show summaries of the clinical data and the flow cytometric analyses, respectively. The flow cytometric data correlated well with disease progression.

Discussion

Findings in our previous analysis of acute-type ATL samples prompted our analysis of various clinical subtypes of patients infected with HTLV-I to examine whether the CD3 versus CD7 profile reflects the progression of oncogenesis in HTLV-I-infected cells [17]. Representative flow cytometric data shown in Figure 1A suggested that the CD3 versus CD7 profile changed during disease progression. As the disease stage progressed, the D and L subpopulations increased with concomitant decreases in the CD3^{high}CD7^{high}(H) subpopulation. Figure 1C, a summary of the flow cytometric data of all cases analyzed, reveals that the two-dimensional plot of the proportions of the D versus L subpopulations could divide all cases into three groups. Group 1, the area under the diagonal line, equivalent to 55% of the H subpopulation in which all normal controls were included (Figure S2), contained the majority of HTLV-I ACs. Group 3 was the area beyond 80% of the L subpopulation, and the majority of acute-type cases were included in this group. Group 2, located between Groups 1 and 3 (*i.e.*, less than 55% of the H subpopulation and 80% of the L

subpopulation), included indolent-type (smoldering and chronic) cases and some AC cases. These results suggest that the CD3 versus CD7 expression profile reflects disease stage. Initially, both the D and L subpopulations gradually and simultaneously increased. However, at the clinically advanced stage, the increase in the L subpopulation was prominent. The change is considered to reflect the biological difference between the D and L subpopulations, which needs to be clarified.

In HTLV-I infection, the small clones of infected cells are considered to coexist from the AC stage [19,20]. A selected clone from the multiple small clones then grows and progresses to the malignant state, and the emergence of a dominant clone indicates disease progression in ATL [19,20]. As shown in Figure 2B–D, major bands suggesting dominant clones were evident in patients with progressed clinical subtypes or those in the advanced group in the CD3 versus CD7 profile, and major bands existed exclusively in the D and L subpopulations. These data also support the idea that increases in the D and L subpopulations correlate with the progression of disease stage. AC cases in Group 2 had high HTLV-I proviral loads (>4%; Figure 1B) and clear major bands were observed by inverse long PCR in these cases (Figure 2B, right). Sasaki *et al.* reported that two cases of HTVL-I AC with oligoclonal bands on Southern blots and high VLs (20%) had progressed to ATL by 4 and 3.5 years later [21]. The two cases may correspond to HTLV-I AC in Group 2 proposed in our study. In fact, two cases of ACs in our series that were included in Group 2 progressed to smoldering ATL (Figure 4A). AC cases in Group 2 could be regarded as advanced carriers. Our flow cytometric analysis could apparently discriminate high-risk AC cases from stable ones. Follow-up analysis of these cases is warranted to determine whether AC cases included in Group 2 progress to ATL. Flow cytometric data for these AC cases included in Group 2 (Figure 1A and 1C) were similar to those for indolent ATL cases in Group 2. These ACs in Group 2 can be considered essentially the same as smoldering ATL cases. Some of the ACs categorized according to Shimoyama's criteria should in fact be separated and regarded as a subtype together with at least some of the smoldering ATL cases.

Iwanaga *et al.* reported that high HTLV-I proviral load (>4%) in whole PBMCs was a risk factor for progression to ATL [13]. In Figure 1B, the ACs with VLs>4% were distributed between Groups 1 and 2. These findings suggest that not all ACs with high VLs are currently in an advanced stage, although they may have the potential to develop ATL in the future.

In general, the categorization by flow cytometric profile correlated well with the current classification of clinical subtypes, with some exceptional cases of acute-type and smoldering-type disease (Figure 3). The only manifestation of three smoldering cases categorized in Group 1 was skin lesions; they fell into Group 1 because they showed minimal abnormalities in peripheral blood [22]. Three acute-type ATL cases categorized in Group 2 had indolent clinical courses. A diagnosis of acute-type disease is made when the indolent-type and lymphoma-type are excluded, according to Shimoyama's criteria. The CD3 versus CD7 plot may discriminate the cases that will follow an indolent clinical course from the aggressive acute-type ATL.

The VL in each subpopulation indicated that HTLV-I-infected cells were relatively concentrated in the D and L subpopulations (representative data are shown in Figure 2A). These data are consistent with downregulation of CD3 and CD7 being relevant to HTLV-I infection, although cells without HTLV-I infection may also contribute to this change to some extent, as a substantial subpopulation of T cells has been reported to be CD7-deficient under physiological [23,24] and certain pathological conditions,

— 149 —

including autoimmune disorders and viral infection [25–29]. To more precisely analyze phenotypic changes in HTLV-I-infected cells, markers that indicate HTLV-I infection should be incorporated in future studies.

A summary of this study is shown in Figure 5. In the CD3 versus CD7 profile, most AC cases were included in Group 1, in which the D and L subpopulations were relatively small. Consistent with disease progression to smoldering- and chronic-type ATL, a decrease in the H subpopulation and increases in the D and L subpopulations occur (Group 2). In this step, increases in the sizes of clones in the D and L subpopulations are observed. Further expansion of the leukemic clone results in progression to acute-type ATL in which the L subpopulation has expanded (Group 3). According to a study by Yamaguchi et al., the natural course of ATL is to progress from the HTLV-I carrier state through the intermediate state, smoldering ATL, and chronic ATL, and finally to the acute ATL, indicating a process of multistage leukemogenesis [19]. We consider this study to successfully link the progressive clinical status and phenotypic changes in HTLV-I-infected cells. However, the way in which this profile reflects multistep oncogenesis in HTVL-I infection at the molecular level remains unclear. Further molecular analyses of the three subpopulations will help in understanding the mechanism(s).

Supporting Information

Figure S1 Representative flow cytometric analysis of an HTLV-I asymptomatic carrier (patient no. 32). The CD3 versus CD7 plot of CD4$^+$ cells was constructed according to the gating procedure shown in this figure. In the plot, we designated three subpopulations: H (CD3^{high}CD7^{high}), D (CD3^{dim}CD7^{dim}), and L (CD3^{dim}CD7^{low}).
(PPTX)

Figure S2 A two-dimensional plot of 10 normal controls showing the percentage of the D and L subpopulations. (PPTX)

Figure S3 Southern blot analysis of clonal integration of the HTLV-I provirus. Representative data (AC, No. 34) are shown. In EcoRI or PstI digestion, a band indicated by a red arrow represents the monoclonal integration of the provirus. The band pattern indicates that two major clones coexist. This analysis was performed by a commercial laboratory (SRL, Tokyo, Japan). (PPTX)

Table S1 Clinical data in a case of chronic-type ATL (No. 53). Proportion of abonormal lymphocytes in the preipheral blood WBC were evaluated by morphological exmanination. LDH: Lactate dehydrogenase (normal range, 120–240 U/L) sIL-2R: soluble interleukin-2 receptor (normal range, 122–496 U/ml). (XLSX)

Acknowledgments

Author Contributions

Conceived and designed the experiments: KT AT KU. Performed the experiments: SK YT. Analyzed the data: EW NW TI NO. Contributed reagents/materials/analysis tools: MI MT KU NO. Wrote the paper: SK KU.

References

1. Yoshida M, Miyoshi I, Hinuma Y (1982) Isolation and characterization of retrovirus from cell lines of human adult T-cell leukemia and its implication in the disease. Proc Natl Acad Sci U S A 79: 2031–2035.
2. Osame M, Usuku K, Izumo S, Ijichi N, Amitani H, et al. (1986) HTLV-I associated myelopathy, a new clinical entity. Lancet 1: 1031–1032.
3. Mochizuki M, Watanabe T, Yamaguchi K, Takatsuki K, Yoshimura K, et al. (1992) HTLV-I uveitis: a distinct clinical entity caused by HTLV-I. Japanese journal of cancer research : Gann 83: 236–239.
4. Proietti FA, Carneiro-Proietti AB, Catalan-Soares BC, Murphy EL (2005) Global epidemiology of HTLV-I infection and associated diseases. Oncogene 24: 6058–6068.
5. Yamaguchi K, Watanabe T (2002) Human T lymphotropic virus type-I and adult T-cell leukemia in Japan. International journal of hematology 76 Suppl 2: 240–245.
6. Murphy EL, Hanchard B, Figueroa JP, Gibbs WN, Lofters WS, et al. (1989) Modelling the risk of adult T-cell leukemia/lymphoma in persons infected with human T-lymphotropic virus type I. International journal of cancer Journal international du cancer 43: 250–253.
7. Shimoyama M (1991) Diagnostic criteria and classification of clinical subtypes of adult T-cell leukaemia-lymphoma. A report from the Lymphoma Study Group (1984–87). Br J Haematol 79: 428–437.
8. Tsukasaki K, Hermine O, Bazarbachi A, Ratner L, Ramos JC, et al. (2009) Definition, prognostic factors, treatment, and response criteria of adult T-cell leukaemia-lymphoma: a proposal from an international consensus meeting. J Clin Oncol 27: 453–459.
9. Takasaki Y, Iwanaga M, Imaizumi Y, Tawara M, Joh T, et al. (2010) Long-term study of indolent adult T-cell leukemia-lymphoma. Blood 115: 4337–4343.
10. Hisada M, Okayama A, Shioiri S, Spiegelman DL, Stuver SO, et al. (1998) Risk factors for adult T-cell leukemia among carriers of human T-lymphotropic virus type I. Blood 92: 3557–3561.
11. Imaizumi Y, Iwanaga M, Tsukasaki K, Hata T, Tomonaga M, et al. (2005) Natural course of HTLV-1 carriers with monoclonal proliferation of T lymphocytes ("pre-ATL") in a 20-year follow-up study. Blood 105: 903–904.
12. Kamihira S, Atogami S, Sohda H, Momita S, Yamada Y, et al. (1994) Significance of soluble interleukin-2 receptor levels for evaluation of the progression of adult T-cell leukemia. Cancer 73: 2753–2758.
13. Iwanaga M, Watanabe T, Utsunomiya A, Okayama A, Uchimaru K, et al. (2010) Human T-cell leukemia virus type I (HTLV-1) proviral load and disease progression in asymptomatic HTLV-1 carriers: a nationwide prospective study in Japan. Blood 116: 1211–1219.
14. Okamoto T, Ohno Y, Tsugane S, Watanabe S, Shimoyama M, et al. (1989) Multi-step carcinogenesis model for adult T-cell leukemia. Japanese journal of cancer research : Gann 80: 191–195.
15. Matsuoka M, Jeang KT (2007) Human T-cell leukaemia virus type 1 (HTLV-1) infectivity and cellular transformation. Nat Rev Cancer 7: 270–280.
16. Yoshida M (2010) Molecular approach to human leukemia: isolation and characterization of the first human retrovirus HTLV-1 and its impact on tumorigenesis in adult T-cell leukemia. Proceedings of the Japan Academy Series B, Physical and biological sciences 86: 117–130.
17. Tian Y, Kobayashi S, Ohno N, Isobe M, Tsuda M, et al. (2011) Leukemic T cells are specifically enriched in a unique CD3(dim) CD7(low) subpopulation of CD4(+) T cells in acute-type adult T-cell leukemia. Cancer science 102: 569–577.
18. Sugamura K, Fujii M, Kannagi M, Sakitani M, Takeuchi M, et al. (1984) Cell surface phenotypes and expression of viral antigens of various human cell lines carrying human T-cell leukemia virus. International journal of cancer Journal international du cancer 34: 221–228.
19. Yamaguchi K, Kiyokawa T, Nakada K, Yul LS, Asou N, et al. (1988) Polyclonal integration of HTLV-I proviral DNA in lymphocytes from HTLV-I seropositive individuals: an intermediate state between the healthy carrier state and smoulding ATL. British journal of haematology 68: 169–174.
20. Mortreux F, Gabet AS, Wattel E (2003) Molecular and cellular aspects of HTLV-1 associated leukemogenesis in vivo. Leukemia : official journal of the Leukemia Society of America, Leukemia Research Fund, UK 17: 26–38.
21. Sasaki D, Doi Y, Hasegawa H, Yanagihara K, Tsukasaki K, et al. (2010) High human T cell leukemia virus type-1(HTLV-1) provirus load in patients with HTLV-1 carriers complicated with HTLV-1-unrelated disorders. Virology journal 7: 81.
22. Setoyama M, Katahira Y, Kanzaki T (1999) Clinicopathologic analysis of 124 cases of adult T-cell leukemia/lymphoma with cutaneous manifestations: the smouldering type with skin manifestations has a poorer prognosis than previously thought. The Journal of dermatology 26: 785–790.
23. Reinhold U, Abken H (1997) CD4+ CD7- T cells: a separate subpopulation of memory T cells? J Clin Immunol 17: 265–271.

— 150 —

24. Reinhold U, Abken H, Kukel S, Moll M, Muller R, et al. (1993) CD7- T cells represent a subset of normal human blood lymphocytes. J Immunol 150: 2081–2089.

25. Aandahl EM, Quigley MF, Moretto WJ, Moll M, Gonzalez VD, et al. (2004) Expansion of CD7(low) and CD7(negative) CD8 T-cell effector subsets in HIV-1 infection: correlation with antigenic load and reversion by antiretroviral treatment. Blood 104: 3672–3678.

26. Autran B, Legac E, Blanc C, Debre P (1995) A Th0/Th2-like function of CD4+CD7- T helper cells from normal donors and HIV-infected patients. J Immunol 154: 1408–1417.

27. Legac E, Autran B, Merle-Beral H, Katlama C, Debre P (1992) CD4+CD7-CD57+ T cells: a new T-lymphocyte subset expanded during human immunodeficiency virus infection. Blood 79: 1746–1753.

28. Schmidt D, Goronzy JJ, Weyand CM (1996) CD4+ CD7- CD28- T cells are expanded in rheumatoid arthritis and are characterized by autoreactivity. J Clin Invest 97: 2027–2037.

29. Willard-Gallo KE, Van de Keere F, Kettmann R (1990) A specific defect in CD3 gamma-chain gene transcription results in loss of T-cell receptor/CD3 expression late after human immunodeficiency virus infection of a CD4+ T-cell line. Proc Natl Acad Sci U S A 87: 6713–6717.

— 151 —

Mutations for decreasing the immunogenicity and maintaining the function of core streptavidin

Kyohei Yumura,[1,2] Mihoko Ui,[2] Hirofumi Doi,[3] Takao Hamakubo,[3] Tatsuhiko Kodama,[3] Kouhei Tsumoto,[1,2]* and Akira Sugiyama[3]*

[1]Institute of Medical Science, The University of Tokyo, Minato-ku, Tokyo 108-8639, Japan

[2]Department of Medical Genome Sciences, Graduate School of Frontier Sciences, The University of Tokyo, Kashiwa 277-8562, Japan

[3]Research Center for Advanced Science and Technology, The University of Tokyo, Komaba, Tokyo 153-8904, Japan

Abstract: The defining property of core streptavidin (cSA) is not only its high binding affinity for biotin but also its pronounced thermal and chemical stability. Although potential applications of these properties including therapeutic methods have prompted much biological research, the high immunogenicity of this bacterial protein is a key obstacle to its clinical use. To this end, we have successfully constructed hypoimmunogenic cSA muteins in a previous report. However, the effects of these mutations on the physicochemical properties of muteins were still unclear. These mutations retained the similar electrostatic charges to those of wild-type (WT) cSA, and functional moieties with similar hydrogen bond pattern. Herein, we performed isothermal titration calorimetry, differential scanning calorimetry, and sodium dodecyl sulfate–polyacrylamide gel electrophoresis to gain insight into the physicochemical properties and functions of these modified versions of cSA. The results indicated that the hypoimmunogenic muteins retained the biotin-binding function and the tetramer structure of WT cSA. In addition, we discuss the potential mechanisms underlying the success of these mutations in achieving both immune evasion and retention of function; these mechanisms might be incorporated into a new strategy for constructing hypoimmunogenic proteins.

Keywords: streptavidin; low immunogenicity; protein engineering; thermodynamic analysis; isothermal titration calorimetry; differential scanning calorimetry; therapeutic protein

Introduction

Core streptavidin (cSA), a protein from *Streptomyces avidinii*, is well known to have an extremely strong binding affinity to biotin ($K_D \sim 10^{-14}$M).[1,2] cSA is also highly resistant to heat,[3,4] denaturants,[5] and proteolysis.[6,7] Because of its unique properties, cSA has been put to practical use in various areas, including biochemistry,[8] and shows therapeutic potential. One possible therapeutic use is in a pretargeting system for drug delivery.[9] However, the immunogenicity of this bacteria-derived protein is an obstacle to its clinical
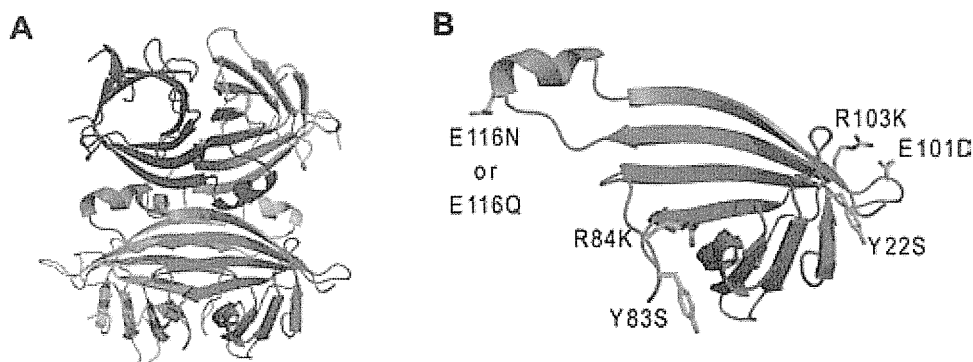
Figure 1. The crystal structure and mutated residues of cSA. (A) Tetrameric structure of cSA WT (from Ref. 20). (B) Mutated residues are indicated as stick forms in a monomeric subunit. All mutations were induced at surface residues not directly involved in either biotin binding or tetramerization.

application.[10–12] One of the most successful approaches for reducing immunogenicity[13,14] is that used for humanizing antibodies.[15] Although grafting sequences from the human homolog into a target protein can reduce the immunogenicity of the resulting hybrid molecule, this strategy cannot be applied to cSA because its human counterpart has not yet been found.

Site-directed mutagenesis is another strategy for reducing the immunogenicity of nonhuman proteins.[16,17] Previous reports have suggested that the immunogenicity of nonhuman proteins was decreased through the elimination of charged or aromatic residues on B-cell epitopes by the replacement of these residues mainly with alanine.[16,17] This mutagenesis strategy has been applied successfully to cSA.[18] Because charged and aromatic residues on the protein surface are considered to be important for immune recognition of proteins including cSA, these residues not directly involved in biotin binding or tetramerization were mutated.[18] This method diminished the immunoreactivity of the mutated cSA to murine and human antistreptavidins, because some of these mutations, especially those at Y83, involved key epitopes for immune recognition.[16] However, the mutations also increased the dissociation rate from biotin,[16] suggesting that the biotin-binding function was reduced. The relationship between the structure and function of cSA seems to be strict,[19] and some mutations reportedly have led to dimerization, destabilization, and decreased binding activity of cSA.[19] Therefore, strategies for mutagenesis of cSA should be considered carefully in regard to both the target residues and those to be substituted.

We also previously performed site-directed mutagenesis of various charged and aromatic residues of cSA that were proposed to be involved in its immune recognition (Fig. 1)[20] and designed the hypoimmunogenic muteins. The immunoreactivities of these muteins against crab-eating monkey antiserum were evaluated by surface plasmon resonance

(Table I and Supporting Information Fig. S1).[21,22] The immunogenicity analyses about T-cell epitope were performed in silico model (Supporting Information Table S1).[22–25] Some muteins had exceedingly low immunoreactivities and the number of T-cell epitope was decreased. However, the effects of these mutations on the physicochemical properties and functions of the resulting cSA muteins had not been studied enough previously. Furthermore, mutations induced here are different from alanine. These mutations, except for E116N and E116Q, are considered to retain similar electrostatic charges to those of the wild-type (WT) residues and have functional moieties that form similar hydrogen bonds (Table I).[22] Here, we performed thermodynamic analyses to reveal the functions of these cSA muteins and the effects of mutations from a biophysical viewpoint. We evaluated the interaction with biotin by using isothermal titration calorimetry (ITC) and assessed thermodynamic stability by using differential scanning calorimetry (DSC) and sodium dodecyl sulfate–polyacrylamide gel electrophoresis (SDS–PAGE). Our results showed that all of the eight muteins we tested bound biotin in the same manner as does WT cSA, and all muteins maintained the thermodynamic

Table I. *Mutated Residues and the Immunoreactivities of the Resulting Muteins*[a]

Mutein	Mutated residue(s)	Relative immunoreactivity to wild-type cSA (%)
072	Y83S	17
001	R84K	61
083	E116N	126
091	E116Q	113
030	Y83S, R84K, E116N	11
040	Y83S, R84K, E116Q	7
314	Y22S, Y83S, R84K, E101D, R103K, E116N	1
414	Y22S, Y83S, R84K, E101D, R103K, E116Q	1

[a] From Ref. 22.

Low Immunogenic Core Streptavidin Muteins

stabilities of the WT form. The present results suggest that the strategy of mutating surface target sites by preserving electrostatic charge and functional moieties prevents immune recognition while maintaining the structure and function of cSA. This strategy may offer an innovative method for constructing hypoimmunogenic muteins of other proteins for therapeutic applications.

Results

Asymmetric field-flow fractionation–multiangle light scattering analyses of mutant cSAs

Recombinant cSA WT and the muteins listed in Table I were expressed in *Escherichia coli* Rosetta2 (DE3) cells as insoluble forms and were refolded to obtain cSA tetramers by using stepwise dialysis as described previously, with slight modification.[26] Size-exclusion chromatography showed single peaks for all of these proteins except mutein 083, which had a shoulder peak (Supporting Information Fig. S2); this shoulder peak was collected as mutein 083′. Field-flow fractionation–multiangle light scattering (FFF-MALS) analyses to evaluate the molecular sizes and weights of the various cSAs showed that the main peaks identified on size-exclusion chromatography had molecular weights consistent with that of tetrameric cSA WT and that, compared with cSA WT, muteins 314 and 414 might have larger molecular radii in the absence of biotin (Supporting Information Fig. S3).

ITC analyses of cSAs

Because biotin-binding activity is a primary, characteristic property of cSA, we used ITC to measure the thermodynamics of biotin-binding among the hypoimmune muteins [Fig. 2(A)]. The WT form and all of the cSA muteins had very strong binding constants $(K_a > 10^{10}~\mathrm{M}^{-1})$ that exceeded the measurement limit of ITC. We note that the values of stoichiometry N were found in the range 1.0–1.2 in all the constructs examined, except that of mutein 083′ (N = 0.8) [Fig. 2(B)]. The binding enthalpies (ΔH_{bind}s) were similar among cSA WT and all muteins (Table II). Therefore, the ITC analyses implied that all muteins other than 083′ had the same biotin-binding characteristics as those of cSA WT.

DSC analyses of cSAs

Thermal stability is an important factor for therapeutic proteins, such as the antibody fragment single-chain Fv.[27] To investigate the thermal stabilities of various cSAs, DSC analyses were carried out. The denaturation temperature (T_{M}) was estimated as the peak top of heat capacity curves. Accordingly, the T_{M}s of cSA WT and the hypoimmunogenic muteins were higher when biotin was bound than in its absence [Fig. 3(A)]. The T_{M}s of muteins 314 and 414 were lower than that of WT in both the absence and

presence of biotin. In comparison, the T_{M}s of muteins 083, 030, and 314, which all contain the mutation E116N, were greatly decreased compared with that of cSA WT, whereas those of muteins 001 and 091 were increased (Table III). Only mutein 083′ yielded multiple peaks on DSC analysis [Fig. 3(B)], indicating that its components contained several tetrameric structures. Although the T_{M}s of the hypoimmunogenic muteins were lower than that of cSA WT (Table III), destabilization was negligible, and all muteins demonstrated sufficient thermal stability under the biological condition.

SDS–PAGE analyses of cSAs

To analyze the thermal and chemical stabilities of the hypoimmunogenic muteins in more detail, we performed SDS–PAGE analyses of the various cSAs with stepwise heating from 45 to 95 °C.[28,29] Streptavidin retains its tetrameric structure even during SDS–PAGE after heating of samples at low temperature.[28,29] The tetrameric band in SDS–PAGE dissociates to a monomeric band only after heating samples at high temperatures thus indicating the thermal stability of streptavidin.[28,29]

Stepwise increases in the sample-heating temperature were associated with progressive migration from high- to low-molecular-weight bands (Fig. 4). The temperatures at which this migration began coincided well with the denaturation temperature determined from the DSC data [Fig. 4(A) and Supporting Information Fig. S6]. Unlike cSA WT and all other muteins, mutein 083′ showed multiple bands at low temperatures [Fig. 4(B)], indicating that this sample may contain several different oligomeric assemblies. The ease with which the high-molecular-weight bands and their migration temperatures could be appreciated indicated that the cSA muteins had sufficient thermal and chemical stability for this analysis, thus indicating the considerable stabilities of cSAs. However, all muteins except cSA WT, mutein 001, and mutein 091 yielded faint low-molecular-weight bands at low temperatures [Fig. 4(A) and Supporting Information Fig. S6), suggesting that the induced mutations slightly decreased the muteins' chemical stability to the denaturant SDS.

Discussion

Few previous studies have investigated the biophysical properties of cSA muteins in detail. Here, we assessed the thermodynamic properties of several cSA muteins that have low immunoreactivities.

ITC implied that biotin-binding activity was similar among cSA WT and all of the muteins we evaluated (Table II). The migrations of T_{M} due to biotin binding were consistent with those of previous reports (Table III).[3,4] SDS–PAGE analysis showed considerable stabilities (Fig. 4). Because cSA
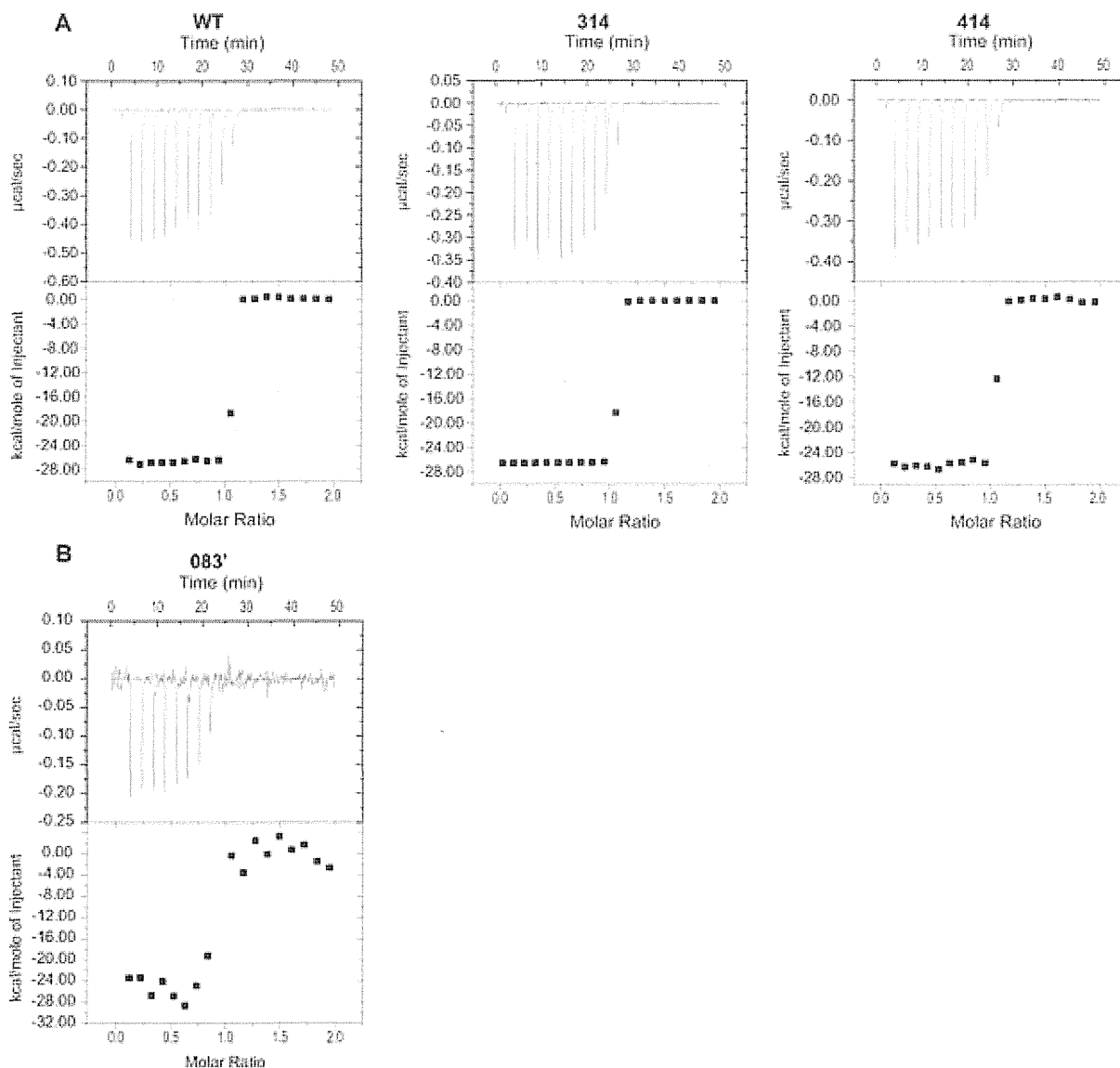
Figure 2. Results of ITC. K_a exceeded the measurement limit of ITC, and ΔS could not be calculated. (A) cSA WT (left); mutein 314 (middle); and mutein 414 (right). (B) 083'.

requires a strict tetrameric structure for high biotin-binding affinity,[19] we concluded that the induced mutations do not disrupt the conformational relationships required for biotin binding. While the R84I mutation has been reported to cause decreased biotin-binding activity compared with that of cSA WT,[18] the R84K variation (mutein 001) did not radically affect K_a or ΔH_{bind} in the current study. This difference may reflect differences in electrostatic charge and functional moieties between isoleucine and lysine. Lysine is similar in electrostatic charge to arginine and likewise carries N—H bonds in its side chain, which enables it to form similar hydrogen bonds. In contrast, isoleucine is apparently unable to form hydrogen bonds because it carries only C—H bonds in its side chain.

The mutation E116N (mutein 083) greatly destabilized the resulting cSA protein in stability analyses (Table III), and mutein 083' showed depression of bind-

ing stoichiometry and tetramerization [Figs. 2(B), 3(B), and 4(B)]. In contrast, the mutation E116Q (mutein 091) stabilized the protein (Table III and Supporting Information Fig. S6). This pronounced difference between mutations at E116 and other mutations also seems to reflect the differences in electrostatic

Table II. *Results of ITC*

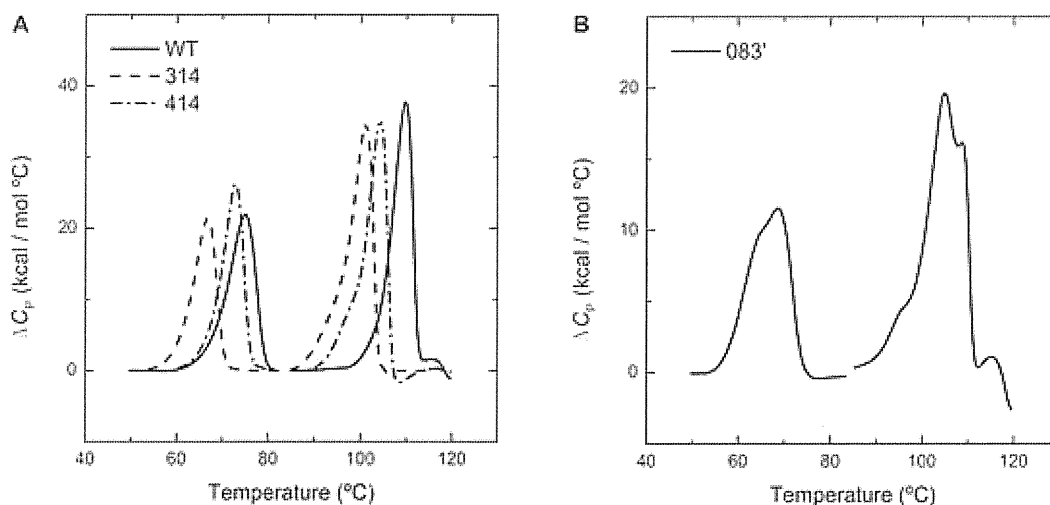| Mutein	Stoichiometry (N)	ΔH_{bind} (kcal mol^{-1})
WT	1.0	−26.7
072	1.1	−27.3
001	1.0	−25.3
083	1.1	−25.2
083'	0.8	−25.4
091	1.1	−26.8
030	1.2	−26.2
040	1.1	−27.8
314	1.0	−26.6
414	1.0	−26.0

Figure 3. Results of DSC analysis in the absence and presence of biotin. The denaturation temperature was increased in the presence of biotin. (A) cSA WT, mutein 314, and mutein 414. (B) Mutein 083', which showed multiple peaks.

charge and functional moiety (carbamoyl group, $-CONH_2$) from those of the WT residue, glutamic acid (carboxyl group, $-COOH$). Our analysis of crystal structural data indicated that the loop and helix near E116 contacts two interfaces of the cSA tetramer (Fig. 5), and mutation of W120 on this helix to lysine was reported to cause dimerization of cSA.[30] Although the mutations E116N and E116Q apparently maintain the conformational structure of cSA, changes in electrostatic charge and functional moieties in this region may alter the thermodynamic stability and tetramerization of the resulting mutein. Therefore, our data regarding R84 and E116 strongly suggest that mutations that preserve the electrostatic charge of the original residues and their functional moieties for hydrogen bonds maintain the functions and structures of the proteins for therapeutic application.

Although the cSA muteins seemed to maintain the tetrameric structure of cSA, the T_Ms of cSA muteins decreased in DSC analyses [Fig. 3(C)], and monomer bands appeared even at low sample-heating temperatures in SDS–PAGE analyses (Fig. 4 and Supporting Information Fig. S6) except for muteins 001 (R84K) and 091 (E116Q). This indicated that each of these mutations slightly decreased the thermal and chemical stabilities of the resulting muteins. However, the decreased tetramerization ability of mutein 083 (E116N only) at refolding was rescued by inducing additional mutations (mutein 030; Y83S, R84K, and E116N) (data not shown). The key for successful refolding is achieving a balance between structural collapse and flexibility of unfolded structures during treatment with denaturant.[31] Our current results suggest that the various mutations we induced in cSA did not totally disrupt its tetrameric structure but instead likely "loosened" it. Although this looseness slightly decreases the thermal and chemical stabilities of the resulting

mutein, it may increase the flexibility of unfolded structures during exposure to denaturants and improve the refolding efficiency. The FFF–MALS analyses of muteins 314 and 414 indicated larger molecular radii in the absence of biotin (Supporting Information Fig. S3), in support of our hypothesis of increased structural looseness in our cSA muteins.

We constructed cSA muteins that had decreased immunoreactivity but that preserved the tetrameric structures and biotin-binding functions of the WT protein. Previous reports have suggested that human and murine immune systems recognize cSA through a conformational epitope.[18] The mutations induced here were expected to maintain the higher-order structures of cSA; however, these mutations probably also changed the residual structures of side chains exposed on the protein surface. These changes might disrupt the conformation of the cSA epitope and thus achieve immune evasion. In this regard, a low-immunogenicity recombinant of staphylokinase (K35A, E65Q, K74R, D82A, S84A, T90A, E99D, T101S, E108A, K109A, K130T, K135R) had several similar mutations (underlined)[16] to those of

Table III. *Results of DSC Analysis*

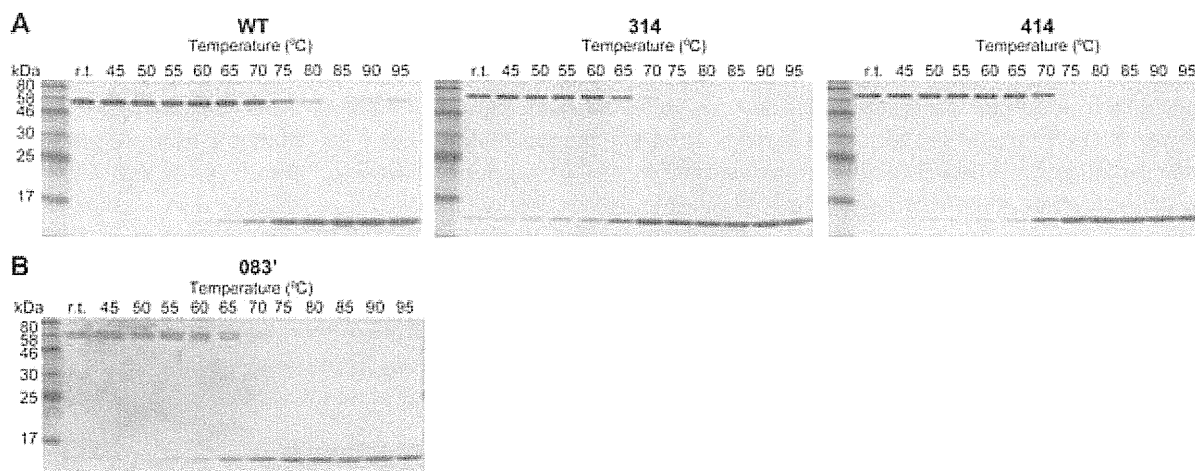| Mutein	T_M (°C)	
	Biotin (−)	Biotin (+)
WT	74.9	109.5
072	73.7	107.8
001	75.7	108.9
083	70.2	109.2
091	76.9	111.1
030	68.2	104.9
040	74.9	107.0
314	66.7	101.0
414	72.9	104.2

— 156 —

Figure 4. Analysis of stability by using SDS–PAGE. Each sample was prepared as a PBS solution and heated for 3 min at the indicated temperature. (A) cSA WT (left), mutein 314 (middle), and mutein 414 (right). (B) Mutein 083′ showed multiple bands at low temperatures.

our hypoimmunogenic cSA muteins. In contrast, the single mutations E116N and E116Q (muteins 083 and 091) increased the immune response to these cSAs (Table I), perhaps due to unexpected effects of structural or thermodynamic changes.

The increased immunoreactivities of muteins 083 and 091 were ameliorated by inducing additional mutations (those in muteins 030, 040, 314, and 414) (Table I). This outcome indicates that looseness of the tetrameric structure might also contribute to increasing immune evasion. This looseness we allude to may generate mobility in the epitope and increase the energy loss associated with antibody binding to prevent immune recognition. Furthermore, the looseness may also contribute to the immunoreactivity correlated to T-cell epitope. It is reported that the high resistance to the lysosomal proteolysis controlled the amount of T-cell epitope and favored its presentation to antigen-presenting cells for longer period, resulting the enhanced immunogenicity of the antigen.[32–34] The decreased stability of cSAs we discussed here may weaken the immunoreactivity of T-cells. However, in this view point, the immunogenicity *in vivo* animal models should be considered, because cSAs become substantially stable in the presence of biotin.

The current study showed that all of our muteins maintained the tetramic structure and functions of cSA WT. We propose that mutein 314 and 414 are the candidates for therapeutic applications. Furthermore, in at least cSAs, our findings also might suggest a new strategy for constructing hypoimmunogenic muteins, in which mutations are induced at charged or aromatic residues on the surface of the target protein; the mutations induced should preserve the electrostatic charge and functional moieties of the WT residues. Consequently, these mutations maintain high-order structures and

functions while modifying the residual structures on the surface and generating structural looseness in the resulting protein that leads to immune evasion. Viruses such as picornaviruses are known to escape antibody recognition through substitutions of surface-exposed residues;[35] this scenario may be somewhat analogous to the strategy we propose here. Unlike previous strategies such as the construction of chimeric antibodies,[15] our current design does not require knowledge of the human counterpart to a target protein. For therapeutics including pretargeting method, we expect that this design will be applied to the other biotin-binding protein such as rhizavidin, the dimeric avidin,[36] or other various proteins, and that the immunogenicity of those designed proteins will be evaluated using animal models.
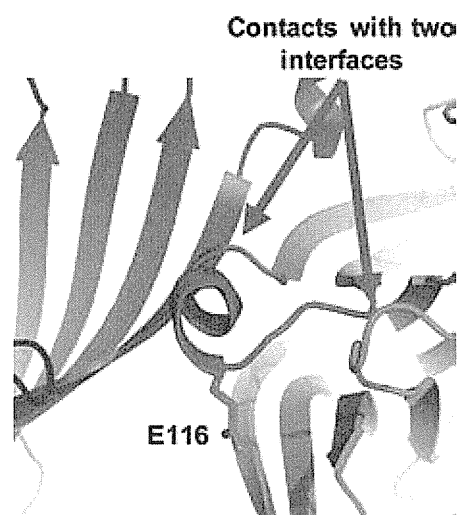

Figure 5. The loop and helix (magenta) near cSA E116 (from Ref. 20) on the interfaces of the tetramer (blue and cyan).

To date, site-directed mutageneses have been performed only to eliminate B-cell epitopes mainly by using alanine,[16,17] and there are no reliable methodologic guidelines for retaining function and structure in the mutated protein. Our current strategy warrants confirmation through its application to other nonhuman proteins with therapeutic potential.

Materials and Methods

Materials

pET28b vector was obtained from Novagen (Darmstadt, Germany). Tetramethylethylenediamine, bromophenol blue, and 30% (w/v)-acrylamide/bis (37.5:1) mixed Solution was purchased from Nacalai Tesque (Kyoto, Japan). Other chemicals including biotin were purchased from Wako (Osaka, Japan). Primers were synthesized by Operon (Tokyo, Japan).

Cloning, expression, and purification of recombinant proteins

cSA (residues 13–139 of streptavidin) WT and its muteins were cloned into pET28b vector by using forward primer 5'-GCGGAAGCTGGTATCACTG-3' and reverse primer 5'-GCTAGCAGCAGAAGGCTT AAC-3'. A His$_6$-tag was fused to the C-terminus. *E. coli* Rosetta2 (DE3) cells were transformed with cSA plasmids (WT and muteins) and grown at 28 °C in 2 × YT Broth containing 50 µg mL^{-1} kanamycin. Expression was induced with 1.0 mM Isopropyl β-D-1-thiogalactopyranoside at O.D.$_{600}$ = 0.8 and then the cells were cultured at 37 °C. Cells were harvested 18 h later by centrifugation (7000 × g, 10 min, 4 °C) and suspended in a buffer comprising 500 mM NaCl and 20 mM Tris-HCl (pH 8.0 at 4 °C). The suspension was sonicated (model UD-201, TOMY, Tokyo, Japan) followed by centrifugation (6000 × g, 30 min, 4 °C). The pellet containing inclusion bodies was washed with wash buffer (2% Triton X-100 and 50 mM Tris-HCl pH 8.0 at 4 °C), acetone, and water purified by reverse osmosis. The pellet then was suspended in buffer A (6 M guanidinium HCl, 500 mM NaCl, 20 mM Tris-HCl; pH 7.9 at 4 °C) containing 5 mM imidazole, followed by shaking overnight at 4 °C. The supernatant was collected by centrifugation (40,000 × g, 30 min, 4 °C) and loaded onto a Ni-NTA resin (Qiagen, Valencia, CA) equilibrated with buffer A containing 5 mM imidazole. Then, the resin was washed with buffer A containing 5 mM imidazole and then buffer A containing 30 mM imidazole. cSA (WT and muteins) were eluted by using buffer A containing 50 mM imidazole and buffer A containing 300 mM imidazole. Eluates were dialyzed against buffer B (200 mM NaCl, 50 mM Tris-HCl, 1 mM EDTA; pH 8.0 at 4 °C) containing 6 M guanidinium HCl for 12 h followed by dialyses against buffer B containing 3 M guanidi-

nium HCl and 2 M guanidinium HCl for 6 h each and buffer B with 0.4 M L-arginine containing 1 M guanidinium HCl and 0.5 M guanidinium HCl for 12 h each. Then the dialysate was dialyzed three times against buffer B for more than 4 h each, followed by centrifugation (6000 × g, 30 min, 4 °C) and filtration over Millex-GP (0.22 µm, PES, 33 mm, sterile; Millipore, Bedford, MA). The supernatant was concentrated by using Amicon Ultra-15 (Millipore, Bedford, MA) and loaded onto a 26/60 Superdex column (GE Healthcare, Piscataway, NJ) equilibrated with buffer B. Eluate fractions were analyzed by using SDS–PAGE, pooled and stored at 4 °C.

FFF–MALS analyses of cSAs

FFF-MALS analyses for the estimation of protein size and weight were done in a Wyatt Eclipse separation system (Wyatt Technology, Santa Barbara, CA). This instrument was equipped with refractive index and MALS detectors. Protein samples were concentrated to 1.8 mg mL^{-1} and supplemented with excess biotin, when needed. The focused flow rate was 3 mL min^{-1}. Separation was performed by using a cellulose membrane with a nominal molecular weight cutoff of 5 kDa. At the elution step, the channel flow was kept at a constant rate of 1 mL min^{-1} and the cross-flow decreased linearly from 3 to 0 mL min^{-1} in 15 min. Buffer B was used for these analyses. The eluted peaks were detected with a refractive index detector, and the molecular weights of these peaks were calculated by using MALS measurement. Data were analyzed with the program ASTRA ver. 5.3 (Wyatt Technology, Santa Barbara, CA) to determine molecular weights.

ITC analyses of cSAs

The thermodynamics of biotin binding were measured by using a iTC$_{200}$ instrument (MicroCal, Northampton, MA). Purified cSAs were dialyzed against PBS overnight. Biotin was dissolved in the same buffer as that of the cSAs to obtain a 500 µM stock solution. This stock solution was adjusted to a concentration tenfold higher than that of each mutein tested. In a calorimeter cell, 9–20 µM cSAs was titrated with biotin solution at 25 °C. Thermography data were analyzed by using the software package ORIGIN (Light Stone, Tokyo, Japan), and titration curves were fitted to a one-site binding isotherm.

DSC analyses of cSAs

Heat capacity curves were measured by using a VP-DSC ultrasensitive scanning calorimeter (MicroCal, Northampton, MA). The heating rate was 1 K min^{-1}. The sample cell was filled with approximately 0.4 mL of PBS containing 20–50 µM cSA or its muteins. When necessary, samples were supplemented with excess biotin. The data were analyzed by using the software package ORIGIN. The buffer baseline was

subtracted from the raw data, which were normalized by protein concentration to obtain thermodynamic parameters and then fitted to two-state thermal transition models.

SDS–PAGE analyses of cSAs

SDS–PAGE analyses were performed as described previously with slight modification.[28,29] Samples of cSAs were prepared as 6 μL aliquots of 9–12 μM PBS solutions and then heated for 3 min at the indicated temperature by using a GeneAmp 9700 PCR system (Applied Biosystems, Tokyo, Japan). Immediately thereafter, 12 μL of sample buffer (80 mM SDS, 62.5 mM Tris-HCl, 8% glycerol; pH 6.8 at room temperature) and 2 μL of 1 mg mL^{-1} bromophenol blue solution containing 10% glycerol were added to the heated samples. The samples were placed on ice and then loaded onto a 15% polyacrylamide gel containing 0.1% SDS. Electrophoresis was performed at 150 V for 80 min. Gels were stained with 0.5% Coomassie brilliant blue R-250, 50% methanol, and 10% acetic acid for more than 10 min and destained with water.

Acknowledgments

References

1. Chaiet L, Wolf FJ (1964) The properties of streptavidin, a biotin-binding protein produced by streptomycetes. Arch Biochem Biophys 106:1–5.
2. Green NM (1990) Avidin and streptavidin. Methods Enzymol 184:51–67.
3. González M, Bagatolli LA, Echabe I, Arrondo JL, Argaraña CE, Cantor CR, Fidelio GD (1997) Interaction of biotin with streptavidin. Thermostability and conformational changes upon binding. J Biol Chem 272:11288–11294.
4. González M, Argaraña CE, Fidelio GD (1999) Extremely high thermal stability of streptavidin and avidin upon biotin binding. Biomol Eng 16:67–72.
5. Kurzban GP, Bayer EA, Wilchek M, Horowitz PM (1991) The quaternary structure of streptavidin in urea. J Biol Chem 266:14470–14477.
6. Bayer EA, Ben-Hur H, Hiller Y, Wilchek M (1989) Post-secretory modifications of streptavidin. Biochem J 259:369–376.
7. Schechter B, Arnon R, Colas C, Burakova T, Wilchek M (1995) Renal accumulation of streptavidin: potential use for targeted therapy to the kidney. Kidney Int 47:1327–1335.
8. Diamandis EP, Christopoulos TK (1991) The biotin-(strept)avidin system: principles and applications in biotechnology. Clin Chem 37:625–636.
9. Knox SJ, Goris ML, Tempero M, Weiden PL, Gentner L, Breitz H, Adams GP, Axworthy D, Gaffigan S, Bryan K, Fisher DR, Colcher D, Horak ID, Weiner LM (2000) Phase II trial of yttrium-90-DOTA-biotin pretargeted by NR-LU-10 antibody/streptavidin in patients with metastatic colon cancer. Clin Cancer Res 6:406–414.
10. Paganelli G, Chinol M, Maggiolo M, Sidoli A, Corti A, Baroni S, Siccardi A (1997) The three-step pretargeting approach reduces the human anti-mouse antibody response in patients submitted to radioimmunoscintigraphy and radioimmunotherapy. Eur J Nucl Med 24:350–351.
11. Goldenberg D, Sharkey R, Paganelli G, Barbet J, Chatal J (2006) Antibody pretargeting advances cancer radioimmunodetection and radioimmunotherapy. J Clin Oncol 24:823–834.
12. Förster GJ, Santos EB, Smith-Jones PM, Zanzonico P, Larson SM (2006) Pretargeted radioimmunotherapy with a single-chain antibody/streptavidin construct and radiolabeled DOTA-biotin: strategies for reduction of the renal dose. J Nucl Med 47:140–149.
13. Fagnani R, Hagan MS, Bartholomew R (1990) Reduction of immunogenicity by covalent modification of murine and rabbit immunoglobulins with oxidized dextrans of low molecular weight. Cancer Res 50:3638–3645.
14. He XH, Shaw PC, Tam SC (1999) Reducing the immunogenicity and improving the in vivo activity of trichosanthin by site-directed pegylation. Life Sci 65:355–368.
15. Vaswani SK, Hamilton RG (1998) Humanized antibodies as potential therapeutic drugs. Ann Allergy Asthma Immunol 81:105–115.
16. Laroche Y, Heymans S, Capaert S, De Cock F, Demarsin E, Collen D (2000) Recombinant staphylokinase variants with reduced antigenicity due to elimination of B-lymphocyte epitopes. Blood 96:1425–1432.
17. Nagata S, Pastan I (2009) Removal of B cell epitopes as a practical approach for reducing the immunogenicity of foreign protein-based therapeutics. Adv Drug Deliv Rev 61:977–985.
18. Meyer DL, Schultz J, Lin Y, Henry A, Sanderson J, Jackson JM, Goshorn S, Rees AR, Graves SS (2001) Reduced antibody response to streptavidin through site-directed mutagenesis. Protein Sci 10:491–503.
19. Laitinen OH, Hytönen VP, Nordlund HR, Kulomaa MS (2006) Genetically engineered avidins and streptavidins. Cell Mol Life Sci 63:2992–3017.
20. Freitag S, Le Trong I, Klumb L, Stayton PS, Stenkamp RE (1997) Structural studies of the streptavidin binding loop. Protein Sci 6:1157–1166.
21. Subramanian N, Adiga PR (1997) Mapping the common antigenic determinants in avidin and streptavidin. Biochem Mol Biol Int 43:375–382.
22. Kodama T, Hamakubo T, Doi H, Sugiyama A, Tsumoto K (2010) Hypo-immunogenic streptavidin and use thereof. International Patent Application WO/2010/095455 (August 26, 2010).
23. Desmet J, Spriet J, Lasters I (2002) Fast and accurate side-chain topology and energy refinement (FASTER) as a new method for protein structure optimization. Proteins: Struct Funct Genet 48:31–43.
24. Desmet J, Meersseman G, Boutonnet N, Pletinckx J, De Clercq K, Debulpaep M, Braeckman T, Lasters I (2005) Anchor profiles of HLA-specific peptides: analysis by a novel affinity scoring method and experimental validation. Proteins: Struct Funct Bioinf 58:53–69.
25. Kapoerchan V, Wiesner M, Hillaert U, Drijfhout J, Overhand M, Alard P, van der Marel G, Overkleeft H, Koning F (2010) Design, synthesis and evaluation of high-affinity binders for the celiac disease associated HLA-DQ2 molecule. Mol Immunol 47:1091–1097.
26. Tsumoto K, Shinoki K, Kondo H, Uchikawa M, Juji T, Kumagai I (1998) Highly efficient recovery of functional single-chain Fv fragments from inclusion bodies

overexpressed in Escherichia coli by controlled introduction of oxidizing reagent—application to a human single-chain Fv fragment. J Immunol Methods 219: 119–129.

27. Willuda J, Honegger A, Waibel R, Schubiger PA, Stahel R, Zangemeister-Wittke U, Plückthun A (1999) High thermal stability is essential for tumor targeting of antibody fragments: engineering of a humanized anti-epithelial glycoprotein-2 (epithelial cell adhesion molecule) single-chain Fv fragment. Cancer Res 59: 5758–5767.

28. Chivers CE, Crozat E, Chu C, Moy VT, Sherratt DJ, Howarth M (2010) A streptavidin variant with slower biotin dissociation and increased mechanostability. Nat Methods 7:391–393.

29. Chivers CE, Koner AL, Lowe ED, Howarth M (2011) How the biotin-streptavidin interaction was made even stronger: investigation via crystallography and a chimaeric tetramer. Biochem J 435:55–63.

30. Laitinen OH, Airenne KJ, Marttila AT, Kulik T, Porkka E, Bayer EA, Wilchek M, Kulomaa MS (1999) Mutation of a critical tryptophan to lysine in avidin or streptavidin may explain why sea urchin fibropellin adopts an avidin-like domain. FEBS Lett 461:52–58.

31. Tsumoto K, Ejima D, Kumagai I, Arakawa T (2003) Practical considerations in refolding proteins from inclusion bodies. Protein Expr Purif 28:1–8.

32. Delamarre L, Pack M, Chang H, Mellman I, Trombetta ES (2005) Differential lysosomal proteolysis in antigen-presenting Cells determines antigen fate. Science 307: 1630–1634.

33. Delamarre L, Couture R, Mellman I, Trombetta ES (2006) Enhancing immunogenicity by limiting susceptibility to lysosomal proteolysis. J Exp Med 203: 2049–2055.

34. Arancibia S, Del Campo M, Nova E, Salazar F, Becker MI (2012) Enhanced structural stability of Concholepas hemocyanin increases its immunogenicity and maintains its non-specific immunostimulatory effects. Eur J Immunol 42:688–699.

35. Mateu MG (1995) Antibody recognition of picornaviruses and escape from neutralization: a structural view. Virus Res 38:1–24.

36. Helppolainen SH, Nurminen KP, Maatta JAE, Halling KK, Slotte JP, Huhtala T, Limatainen T, Yla-Herttuala S, Airenne KJ, Narvanen, Janis J, Vainiotalo P, Valjakka J, Kulomaa MS, Nordlund HR (2007) Rhizavidin from Rhizohium etli: the first natural dimer in the avidin protein family. Biochem J 405:397–405.

Molecular BioSystems

COMMUNICATION

Structural and thermodynamic characterization of the self-adhesive properties of human P-cadherin†

Shota Kudo,[a] Jose M. M. Caaveiro,[b] Takamitsu Miyafusa,[a] Shuichiro Goda,[c] Keisuke Ishii,[d] Tadashi Matsuura,[d] Yukio Sudou,[d] Tatsuhiko Kodama,[e] Takao Hamakubo[e] and Kouhei Tsumoto*[ab]

Human P-cadherin is a promising therapeutic target against cancer. However, its characterization at the molecular level is still lacking. We report that human P-cadherin associated irreversibly in a distinct dimer configuration. Unexpectedly, the divalent cation Ca^{2+} was not necessary for dimerization, although it greatly stabilized the protein–protein complex.

Cadherins are a large family of cell-surface membrane proteins that mediate intercellular adhesion and maintain solid tissue.[1] Classical cadherins are the largest and best characterized group. They self-associate in a Ca^{2+}-dependent manner during cell–cell adhesion owing to their extracellular cadherin (EC) domains.[2] Dimerization occurs at the N-terminal end by a strand-swap mechanism that involves residues Asp1 and Trp2.

P-cadherin belongs to the classical cadherin family, showing high similarity at the primary sequence level to model proteins E-cadherin and N-cadherin (ESI†, Fig. S1). Human P-cadherin is weakly expressed in the basal layers of stratified epithelia where it regulates tissue maintenance and development, and drives cell proliferation.[1,3] Human P-cadherin is also over-expressed in pancreatic, lung, gastric, and colorectal cancers.[4] Importantly, inhibition of the adhesive properties of P-cadherin by therapeutic antibodies suppresses the growth of primary tumors and their metastatic progression.[5] Although P-cadherin is a promising therapeutic candidate, the protein has not been yet subjected to detailed biochemical and biophysical characterization. To understand the adhesive mechanism of P-cadherin we prepared recombinant forms of the first and second ectodomains (EC12). These two domains constitute the minimum structural element responsible for dimerization in other classical cadherins.[2]

[a] Department of Medical Genome Sciences, The University of Tokyo, Tokyo, 108-8639, Japan. E-mail: tsumoto@ims.u-tokyo.ac.jp; Fax: +81 3-6409-2129; Tel: +81 3-5449-5316
[b] Institute of Medical Sciences, The University of Tokyo, Tokyo, 108-8639, Japan
[c] Faculty of Engineering, Nagasaki University, Nagasaki, 852-8521, Japan
[d] Perseus Proteomics Inc., Komaba, Tokyo, 153-0041, Japan
[e] Research Center for Advanced Science and Technology, The University of Tokyo, Tokyo, 153-8904, Japan
† Electronic supplementary information (ESI) available: Experimental details; sequence alignment; AF4; SAXS; intrinsic fluorescence. See DOI: 10.1039/c2mb25161b
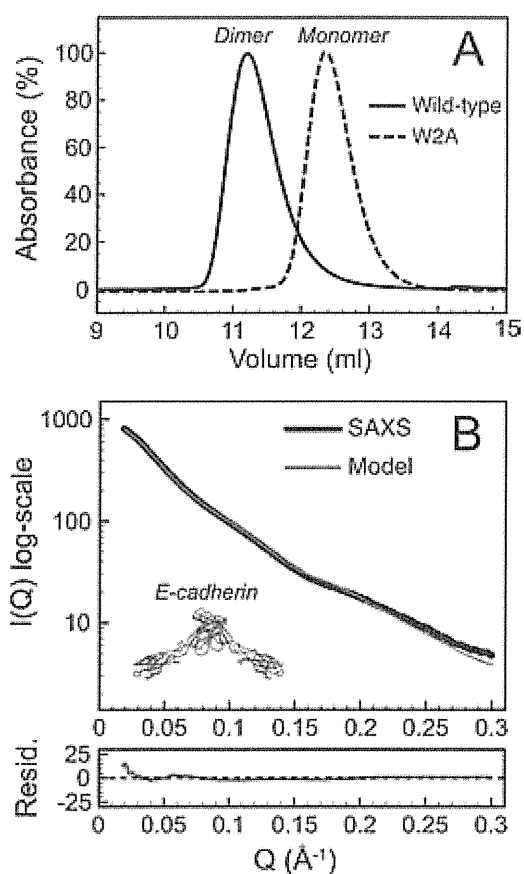
Cloning, expression, and purification of EC12 (residues 1–241) of the mature human P-cadherin were carried out with a pET-SUMO vector as described in ESI.† After purification and cleavage of the N-terminal SUMO-tag we obtained protein >95% homogeneous as judged by SDS-PAGE (not shown). Molecular size was evaluated by analytical size exclusion chromatography (SEC) and asymmetric flow-field flow-fractionation (AF4) (ESI†). Small-angle X-ray scattering (SAXS) data were collected at beamline BL-10C of the Photon Factory in Tsukuba (Japan) as described previously.[6] Thermodynamic analysis carried out by differential scanning calorimetry (DSC) and isothermal titration calorimetry (ITC) is explained in ESI.†

SEC and AF4 were employed to monitor the dimerization state of EC12 in the presence of Ca^{2+} (Fig. 1A; ESI†, Fig. S2A). The SEC profile showed a single and well-resolved peak centered at 11.2 ml. The position of this peak contrasted with that of the mutein EC12-W2A (12.3 ml), a monomeric variant lacking the key residue Trp2 necessary for the dimerization of cadherins.[7] The molecular weight of EC12 was determined by AF4 because the elongated shape of cadherins prevents accurate determination by SEC. The value obtained by AF4 was 43 kDa, a figure compatible with the predicted size of the dimer (53 kDa).

SAXS further revealed the dimeric nature of P-cadherin in solution (Fig. 1B). We found that the experimental SAXS profile of EC12 and the calculated curve of the strand-swap dimer (ss-dimer) of the highly homologous human E-cadherin (PDB entry code 2O72) superimposed well. The excellent agreement between the experimental and calculated curves contrasted with the poor fitting when the monomeric form of E-cadherin was used (ESI†, Fig. S3). In aggregate, SEC, SAXS, AF4, and mutational analysis demonstrated that P-cadherin self-associates in solution in the ss-dimer configuration in a manner analogous to that of E- and N-cadherins.[7]

Ca^{2+} is a cation intimately linked to the assembly of classical cadherins.[2,8] The first and second EC domains of E- and N-cadherin bind three atoms of Ca^{2+} before triggering protein dimerization, and this cation is also necessary for the maintenance of the dimeric state.[9] To examine the effect of Ca^{2+} on the adhesive properties of P-cadherin we followed two alternative procedures. In the first approach, Ca^{2+} ions were removed prior to the association step (before dimerization). Because the protein is expressed with a 12 kDa His_6-SUMO-tag

Fig. 1 Dimerization of P-cadherin. (A) SEC profile of wild-type EC12 (solid line) and mutein W2A (broken line). (B) Experimental SAXS profile of P-cadherin EC12 (black) and theoretical curve of crystallographic ss-dimer of E-cadherin (red) calculated with the program FoXS of the Chimera suite (PDB entry code 2O72).[12] Buffer contained 3 mM Ca^{2+}.

Fig. 2 Dimerization of P-cadherin is largely independent of Ca^{2+}. SEC profiles of samples of EC12 obtained after Ca^{2+}-depletion by two different methodologies: Ca^{2+} was removed before (solid line), or after (broken line) treatment with SUMO protease. Dotted line corresponds to mutein W2A.

at the N-terminal, EC12 remains as a monomer until protease cleavage of the SUMO-tag. This procedure mimicked the activation route of classical cadherins *in vivo*.[2] By incubating the samples with excess EDTA before protease cleavage, we could study the dimerization of EC12 in the absence of Ca^{2+} ions. In the second approach, Ca^{2+} ions were removed with EDTA after the dimerization reaction had proceeded in the presence of Ca^{2+}.

SEC was employed to monitor the self-dimerization of EC12 (Fig. 2). The chromatographic profiles of the two types of Ca^{2+}-depleted samples were essentially identical to each other, and also very similar to that of dimeric EC12 in the presence of Ca^{2+} (see Fig. 1A). We observed a small shoulder corresponding to the monomeric form of the protein. The fraction of the monomeric form estimated from SEC data was very small (<5%). The molecular weight of the major peak determined by AF4 was 53 kDa, a value consistent with the dimeric form of the protein (ESI†, Fig. S2B). The fluorescence spectra of Ca^{2+}-depleted samples indicated that the dimerization site around Trp2 in either structure was essentially identical (ESI†, Fig. S4). Overall, this set of experiments demonstrated that dimerizaton of EC12 was independent of Ca^{2+}. This is an unusual observation in the cadherin family of proteins, and
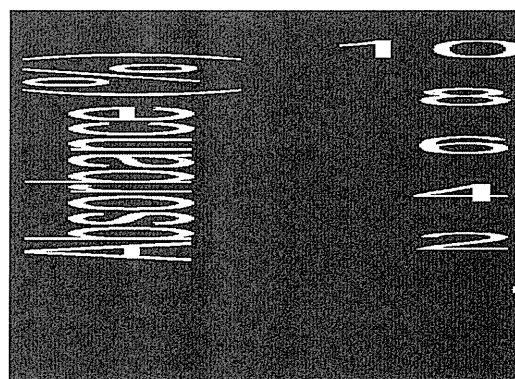
suggested that the self-affinity of P-cadherin is higher than that of homologous cadherins.[9]

The thermodynamic basis for the binding of Ca^{2+} to P-cadherin was determined by ITC and DSC (Fig. 3). Titration of apo-EC12 with Ca^{2+} gave rise to a typical sigmoidal binding isotherm (Fig. 3A). Each molecule of apo-EC12 bound an average of 2.7 atoms of Ca^{2+}. This value was consistent with the three Ca^{2+} ions found in the crystal structures of homologous E- and N-cadherins. This result also validated the methodology employed to remove the Ca^{2+} ions from the protein samples. The binding constant (dissociation constant, K_D) obtained from the fitting procedure was 23 ± 6 μM. Binding of Ca^{2+} to P-cadherin was driven by both favourable enthalpy ($\Delta H_B = -2.6 \pm 0.1$ kcal mol^{-1}) and entropy terms ($-T\Delta S_B = -3.6$ kcal mol^{-1}). These results
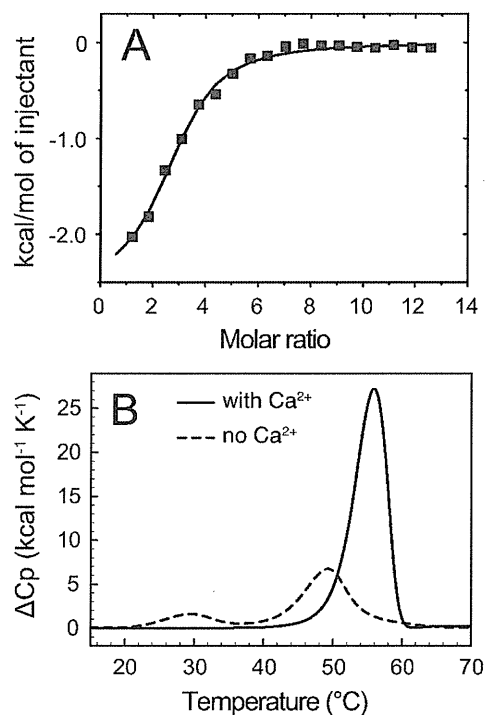

Fig. 3 Thermodynamic analysis. (A) Binding isotherm of Ca^{2+} to apo-EC12. (B) Thermal stability of EC12 in the presence of 3 mM Ca^{2+} (solid line), or Ca^{2+}-depleted samples (broken line).

— 162 —

Table 1 Effect of Ca^{2+} on the stability of P-cadherin

Ca^{2+}	T_{M1} (°C)	ΔH_1 (kcal mol^{-1})	T_{M2} (°C)	ΔH_2 (kcal mol^{-1})
Absent	49.0 ± 0.1	-61 ± 0.3	29.6 ± 0.1	-16 ± 0.5
Present	55.4 ± 0.1	-155 ± 1.0	N.O.^{a}	N.O.

^{a} N.O., not observed.

revealed a complex thermodynamic pattern that did not fit a simple interaction model.[10] We suggest that binding of Ca^{2+} to P-cadherin involved various sources of stabilization, in addition to the electrostatic interaction between Ca^{2+} and protein.

The thermal denaturation profile of EC12 in the absence of Ca^{2+} also displayed a complex pattern (Fig. 3B and Table 1). First, the thermal transition did not obey the classical two-state equation. Instead, the Ca^{2+}-depleted form of P-cadherin gave rise to two separate transitions of variable enthalpy (it is tempting to speculate that each peak could correspond to the individual transition of each domain). The mid-point transitions occurred at temperatures of 49 and 30 °C, respectively, although only the second transition displayed a significant enthalpy change ($\Delta H = -61 \pm 0.3$ kcal mol^{-1}).

In contrast, the presence of Ca^{2+} dramatically altered the thermal profile of EC12. First, the thermogram showed high cooperativity and displayed only one transition. Second, the thermal stability T_M increased by 6 °C when Ca^{2+} was present. And third, the enthalpy of the transition increased significantly under Ca^{2+} conditions ($\Delta H = -155$ kcal mol^{-1}; $\Delta\Delta H = -95$ kcal mol^{-1}). We note that the magnitude of $\Delta\Delta H$ is almost an order of magnitude higher than that determined in analogous experiments with E- and N-cadherin.[9,11] This analysis thus demonstrated the key role of Ca^{2+} in the thermal stabilization of P-cadherin.

We summarize our results in Fig. 4. P-cadherin can adopt three possible configurations in solution: (i) monomer, (ii) flexible dimeric state, and (iii) stable ss-dimer. The monomeric form of P-cadherin is not favoured thermodynamically, and thus dimerizes spontaneously even in the absence of Ca^{2+}. These observations mark a departure from the behaviour of other members of the classical cadherin family, and suggested stronger self-adhesive properties of P-cadherin. We propose that these novel properties arise from differences at the primary sequence level, in particular in the critical N-terminal region. We also speculate that cell–cell adhesion mediated by human P-cadherin is persistent, which could
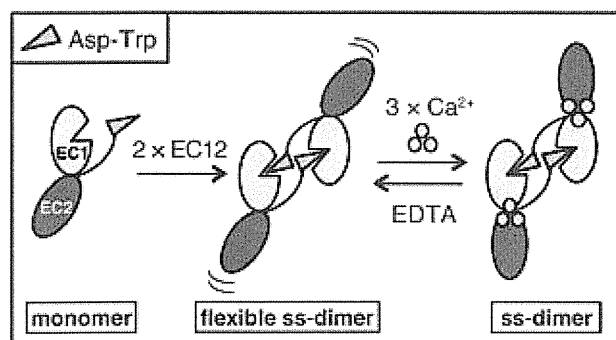
facilitate the attachment of cancer cells expressing high levels of this protein. We hope these results will guide the exploration of therapeutic treatments based on human P-cadherin.

Conclusions

We found that human P-cadherin self-associates in the ss-dimer configuration, similarly to other classical cadherin proteins. Unexpectedly, Ca^{2+} was not necessary for the dimerization of P-cadherin, although it enhanced its thermal stability. Overall, our analysis suggested that P-cadherin possesses stronger adhesive properties than other members of the classical cadherin family.

Abbreviations

EC	Extracellular cadherin
IMAC	Immobilized-metal affinity chromatography
SEC	Size exclusion chromatography
AF4	Asymmetric flow-field flow-fractionation
DSC	Differential scanning calorimetry
ITC	Isothermal titration calorimetry
SAXS	Small-angle X-ray scattering
ss-dimer	Strand-swap dimer

Acknowledgements

Notes and references

1 M. Takeichi, *Development*, 1988, **102**, 639; M. Takeichi, *Annu. Rev. Biochem.*, 1990, **59**, 237; B. D. Angst, C. Marcozzi and A. I. Magee, *J. Cell Sci.*, 2001, **114**, 629.
2 B. Nagar, M. Overduin, M. Ikura and J. M. Rini, *Nature*, 1996, **380**, 360; D. Haussinger, T. Ahrens, T. Aberle, J. Engel, J. Stetefeld and S. Grzesiek, *EMBO J.*, 2004, **23**, 1699; O. J. Harrison, E. M. Corps and P. J. Kilshaw, *J. Cell Sci.*, 2005, **118**, 4123; O. J. Harrison, F. Bahna, P. S. Katsamba, X. Jin, J. Brasch, J. Vendome, G. Ahlsen, K. J. Carroll, S. R. Price, B. Honig and L. Shapiro, *Nat. Struct. Mol. Biol.*, 2010, **17**, 348.
3 R. T. Bryan and C. Tselepis, *J. Urol.*, 2010, **184**, 423.
4 Y. Shimoyama, S. Hirohashi, S. Hirano, M. Noguchi, Y. Shimosato, M. Takeichi and O. Abe, *Cancer Res.*, 1989, **49**, 2128; K. Imai, S. Hirata, A. Irie, S. Senju, Y. Ikuta, K. Yokomine, M. Harao, M. Inoue, T. Tsunoda, S. Nakatsuru, H. Nakagawa, Y. Nakamura, H. Baba and Y. Nishimura, *Clin. Cancer Res.*, 2008, **14**, 6487.
5 C. C. Zhang, Z. Yan, Q. Zhang, K. Kuszpit, K. Zasadny, M. Qiu, C. L. Painter, A. Wong, E. Kraynov, M. E. Arango, P. P. Mehta, I. Popoff, G. F. Casperson, G. Los, S. Bender, K. Anderes, J. G. Christensen and T. VanArsdale, *Clin. Cancer Res.*, 2010, **16**, 5177; H. Yoshioka, S. Yamamoto, H. Hanaoka, Y. Iida, P. Paudyal, T. Higuchi, H. Tominaga, H. Nakagawa, Y. Shiba, K. Yoshida, R. Osawa, T. Katagiri, T. Tsunoda, Y. Nakamura and K. Endo, *Cancer Immunol. Immunother.*, 2012, DOI: 10.1007/s00262-011-1186-0.
6 Y. Hiragi, Y. Seki, K. Ichimura and K. Soda, *J. Appl. Crystallogr.*, 2002, **35**, 1; T. Ueki, Y. Hiragi, M. Kataoka, Y. Inoko, Y. Amemiya, Y. Izumi, H. Tagawa and Y. Muroga, *Biophys. Chem.*, 1985, **23**, 115.
7 K. Tamura, W.-S. Shan, W. Hendrickson, D. R. Colman and L. Shapiro, *Neuron*, 1998, **20**, 1153; E. Parisini, J. M. Higgins, J. H. Liu, M. B. Brenner and J. H. Wang, *J. Mol. Biol.*, 2007, **373**, 401.

Fig. 4 Model of dimerization of P-cadherin. EC12 self-associates irreversibly in the ss-dimer configuration without the need of Ca^{2+}. This form of the ss-dimer can bind up to three Ca^{2+} ions that greatly stabilize the dimeric configuration.

— 163 —

8 C. Ciatto, F. Bahna, N. Zampieri, H. C. VanSteenhouse, P. S. Katsamba, G. Ahlsen, O. J. Harrison, J. Brasch, X. Jin, S. Posy, J. Vendome, B. Ranscht, T. M. Jessell, B. Honig and L. Shapiro, *Nat. Struct. Mol. Biol.*, 2010, **17**, 339; N. Vunnam and S. Pedigo, *Biochemistry*, 2011, **50**, 2973.

9 N. Vunnam, J. Flint, A. Balbo, P. Schuck and S. Pedigo, *Biochemistry*, 2011, **50**, 2951.

10 P. D. Ross and S. Subramanian, *Biochemistry*, 1981, **20**, 3096.

11 N. Vunnam and S. Pedigo, *Biochemistry*, 2011, **50**, 8437; N. Vunnam and S. Pedigo, *Biochemistry*, 2011, **50**, 6959.

12 D. Schneidman-Duhovny, M. Hammel and A. Sali, *Nucleic Acids Res.*, 2010, **38**, W540; E. F. Pettersen, T. D. Goddard, C. C. Huang, G. S. Couch, D. M. Greenblatt, E. C. Meng and T. E. Ferrin, *J. Comput. Chem.*, 2004, **25**, 1605.